Results in Optics 14 (2024) 100604

Contents lists available at ScienceDirect

Results in Optics

journal homepage: www.sciencedirect.com/journal/results-in-optics

Highly sensitive optical fibre Bragg grating contact pressure sensor embedded in a polymer layer: Modelling and experimental validation

C.L. Abeywardena [a], Q. Zhang [a,b], S. Korposh [a,*], S.P. Morgan [a], S. Bull [a], R. Correia [a]

[a] Optics and Photonics Group, Faculty of Engineering, University of Nottingham, Nottingham, NG7 2RD, UK
[b] Department of Engineering, Nottingham Trent University, Nottingham, NG11 8PR, UK

A B S T R A C T

This paper discusses mathematical modelling and experimental validation of a highly sensitive optical fibre Bragg grating (FBG) contact pressure sensor developed for healthcare applications. Bare FBGs are not very sensitive to pressure ($\sim 3 \times 10^{-3}$ nm/MPa) but this can be increased by embedding the FBG in a polymer layer which acts as transducer to convert transverse load (pressure) applied to an axial strain, measured by the FBG sensor. The pressure sensitivity of the FBG sensor depends on the mechanical and physical properties such as Young's modulus, shape and size of the polymer. A finite element analysis (FEA) model is developed to optimise the design parameters of the FBG sensor in order to achieve a high sensitivity. A transfer matrix mathematical formulism is then used to relate the reflection spectrum of the FBG to the strain experienced. Three different shapes, three different sizes and three different polymer materials with different Young's moduli have been simulated and their wavelength sensitivities related to the transverse pressure. According to the simulation results, the pressure sensitivity of a bare FBG can be increased ~ 270 times (0.8179 nm/MPa) by selecting an FBG of 3 mm length, embedding it at the horizontal centre of a polymer layer of Young's modulus of 20 MPa, in the shape of a circular disc with a diameter 5.5 mm and thickness of 1 mm.

1. Introduction

Accurate contact pressure measurement is very important in avoiding pressure injuries caused by being in prolonged contact with mattresses, wheelchairs and prostheses, or through using devices such in dwelling catheters. A pressure ulcer is defined as an area of tissue damage appearing after a prolonged period of inadequate blood supply to the tissue. The main extrinsic causes of pressure ulcers are pressure, friction, humidity and shear forces (Jonsson et al., 2005; Magalhaes, 2007). If the pressure on the arterial side of a tissue exceeds 30–32 mmHg, which is the capillary filling pressure, this may cause tissue death and ulceration (Bhattacharya and Mishra, 2015). In UK, the average daily costs of treating a pressure ulcer are estimated to range from £43 to £374 and mean healing cost per patient ranges from £1214 to £14108 depending on the ulcer category (Dealey et al., 2012). Monitoring of contact pressure can help avoid tissue injury by alerting clinicians when contact pressure is too high or when there has been prolonged contact.

Our research (Correia, 2021; Correia et al., 2018; Hernandez, 2017; Morgan, 2019) is investigating methods of avoiding pressure injury due to endotracheal (ET) intubation in which an endotracheal tube is inserted to the trachea for the purpose of establishing and maintaining an airway to deliver oxygen enriched air or an anaesthetic. In order to achieve a gas seal at the cuff-trachea interface but to avoid tracheal injury, it is recommended that the ET tube cuff is inflated to 20–30 cmH_2O (2–4 kPa) (Touman and Stratakos, 2018). If the contact pressure exceeds the required limit for prolonged periods it may cause various problems such as mucosal/ dermal pressure ulcers, post intubation tracheal stenosis (PITS) and more critical and fatal conditions such as obstructive fibrinous tracheal pseudomembrane (OFTP) (Touman and Stratakos, 2018).

Another healthcare challenge where contact pressure measurement is important is in compression bandaging where it is necessary to obtain and maintain a desired sub bandage pressure during its application and wear. Venous leg ulcers (VLU) are a major cause of morbidity and affect up to 3 % of the adult population in the United States and Europe (Margolis et al., 2002). A study has shown that 87 % of VLU patients are prescribed a recognised compression bandage treatment and 52 % of them were healed (Guest et al., 2018). The mainstay of treatment for established venous insufficiency includes the use of compression to apply external pressure to the lower extremities with the aim of improving venous function (Pfisterer et al., 2014).

According to the World Union of Wound Healing Societies (WUWHS) consensus document for compression in venous leg ulcers (Compression in venous leg ulcers, 2020), bandage systems and compression garments are graded according to the level of compression they produce. WUWHS

* Corresponding author.
E-mail address: s.korposh@nottingham.ac.uk (S. Korposh).

https://doi.org/10.1016/j.rio.2024.100604
Received 8 September 2023; Received in revised form 3 December 2023; Accepted 3 January 2024
Available online 10 January 2024

suggest 4 different levels of pressure applied to the limb. Mild (<20 mmHg ≈ 2.66 kPa), moderate (≥20-40 mmHg ≈ 2.66—5.33 kPa), strong (≥ 40–60 mmHg ≈ 5.33–7.99 kPa) and very strong (>60 mmHg ≈ 7.99 kPa). The required amount of sub bandage pressure is determined by the underlying pathologies as well as the patient's ability to tolerate the compression. For example strong compression is recommended for venous leg ulcer treatment and very strong compression is recommended for lymphoedema (European Wound Management Association (EWMA), 2003). However, these recommendations may again vary depending on the conditions such as their age, patients with arterial insufficiency or cardiac failure. Additionally, depending on the activity level of the patient the applied sub bandage pressure may differ. For example, sub bandage pressure tends to be lowest when patient is resting/lying down and higher peaks could be obtained during exercises (Compression in venous leg ulcers, 2020).

Prosthetics is also another healthcare field application where interface pressure measurements techniques are deployed widely. The pressure measurement at the interface between the stump and the prosthetic socket could provide valuable information in the process of prosthetic socket fabrication, modification and fit (Buis and Convery, 1997). The prime objective of any prosthesis is to provide function in a comfortable manner. However comfort of the prosthesis dependents on the pressure between the socket and the residual limb (Pirouzi et al., 2014). Depending on the type of socket, the interface pressure range between the residual limb and the socket may differ widely. For example Moo *et al.* (Moo et al., 2009) discusses interface pressure profile analysis of two types of sockets, namely the patellar tendon bearing (PTB) socket and hydrostatic socket. According to the study anterior pressure profile of the PTB socket exhibits a pressure range of 50–90 kPa whereas the posterior PTB socket exhibits peak pressure up to 210–230 kPa. Quesada *et al.* (Quesada and Skinner, 1991) discusses in their study of analysis of below knee PTB prosthesis, pressure peaks can go up to 800 kPa for hard sockets.

There is a wide variety of available contact pressure sensors including pneumatic, piezoelectric, resistive, and capacitive technologies. Each of these approaches has drawbacks. For example Barbenel *et al.* (Barbenel and Sockalingham, 1990) developed a device for measuring soft tissue interface pressure consisting of a commercially available electro pneumatic sensor cell attached to 1 m of tubing. The transducer is a piezo resistive pressure sensitive device whose output voltage is proportional to the applied pressure in the range 0–5 kPa. The response is linear and robust, however, it suffers from bulkiness and low flexibility. The sensor cell, tubing and transducer are filled with vegetable oil and this may cause problems such as air bubbles formation during motion and is not suitable in dynamic studies. Steinberg *et al.* (Steinberg and Cooke, 1993) present a method for the measurement of contact pressure using an electro pneumatic sensor that transforms displacement or proximity into change in air pressure. The main drawbacks of this sensor are that it suffers from hysteresis and low sampling rates.

Ferguson-Pell *et al.* (Ferguson-Pell et al., 2000) evaluated a sensor which is commercially available for low interface pressure measurements (Flexiforce, Tekscan). The sensor uses an ink whose electrical resistance changes with the force applied. The main drawbacks highlighted in this study were its poor response and the output drift to the curvature. Buis *et al.* (Buis and Convery, 1997) has also discussed calibration problems encountered while monitoring interface pressures with force sensing resistors (resistive ink 9810F socket, Tekscan). Sensitivity to loading rates and the hysteresis are the main drawbacks obtained for these type of sensors.

Optical fibre sensors offer attractive solutions to a number of measurement challenges faced in healthcare (Correia et al., 2018). Different optical fibre sensing approaches can be applied to physical measurements such as fibre long period grating (Rana et al., 2022; Wong et al., 2019), fibre in-line interferometer (Wu, 2021; Chen, 2020) and fibre Sagnac loop (Culshaw, 2006; Shao, 2019). Amongst these, fibre Bragg gratings (FBGs) offer an attractive solution for healthcare as they offer the opportunity to multiplex multiple sensors (up to 40) on the same optical fibre. Furthermore, they are widely available commercially and the price of interrogation units have been reducing. An FBG consists of a periodic modulation of the refractive index of the core of a single mode optical fibre. An FBG reflects light at a specific wavelength which depends on the period and refractive index of the grating. FBGs can be multiplexed along a single fibre for distributed measurements. Although FBGs are sensitive to strain and temperature, they are less sensitive to pressure with bare FBG sensitivity of about 3.04×10^{-3} nm/MPa (Xu et al., 1993). Nevertheless, FBG sensors can be engineered in a way that pressure can be transduced to axial strain with an increase in its pressure sensitivity.

Wang *et al.* (Wang et al., 2013) describe a FBG force sensor for monitoring contact pressure during compression therapy, consisting of two arrays of FBG entwined in a double helix form. Due to the double helix structure when forces are applied one FBG experience a compression whiles the other experiences elongation. The differential Bragg wavelength shift is used to determine the applied force whereas temperature fluctuation causes a common mode variation which is independent of the force induced differential wavelength shift. This sensor array is immune to temperature and capable of real time distributed sensing of sub-bandage pressure.

Correia *et al.* (Correia, 2016; Correia et al., 2010; Correia et al., 2007) presented a pressure measuring system using an FBG embedded in an polymer layer (epoxy) that transduces the external pressure into strain on the FBG more efficiently. The deformation of the polymer in response to the transverse load results in an axial strain across the FBG. This results in a change in the periodic length of the grating and the refractive index of the FBG over the embedded region. This approach has been used for measuring the contact pressure between an ET tube cuff and the trachea (Correia, 2016). The sensitivity observed was 2.1×10^{-2} nm/kPa which is a factor of 15 greater than a bare FBG.

The pressure response of such a sensor is highly dependent on the physical properties of the polymer layer. Initial designs utilised an epoxy cube (Correia, 2016, 2021), but there is a potential to tailor the sensitivity by utilising different materials, shapes and sizes of the layer. This is one of the key characteristics that should be expected from an ideal contact pressure measurement sensor (Partsch, 2006). An accurate simulation is beneficial to this optimisation process.

In research there are several examples where the FBGs undergo birefringence due to the magnitude of the transverse loading (Gafsi and El-Sherif, 2000; Correia et al., 2006). Therefore, it is important to account for the birefringence in the context of FBGs under transverse pressure. In this paper, finite element analysis (FEA) is used to simulate the stress/strain field along the FBG due to transverse loading. The transfer matrix method is then used to map the FBG strain onto the anticipated reflected spectrum. Hu *et al.* (Hu et al., 2016) presented an FBG simulation for real time evaluation of transverse cracking in cross-ply laminates using the transfer matrix method. Hassoon *et al.* (Hassoon et al., 2015) applied a similar approach to simulate of mode-I delamination detection to determine material strength. Pereira *et al.* (Pereira et al., 2016) developed an FBG FEA tool that provides three different simulations; longitudinal uniform strain, longitudinal non uniform strain and transverse stress. This is a useful approach but for transverse stress simulation, the non-uniformity of the grating is not considered but is replaced by an average strain. Moreover these models have not been used to optimise the design for healthcare applications.

In this research we develop a new model that accounts for the non-unformity of the grating and use this model to optimise the design of FBG based contact pressure sensors for healthcare.

2. Simulation theory of FBG sensor

Light guided in the core of an optical fibre undergoes a Fresnel reflection at each of the grating interfaces where there is a refractive

index change. The light becomes progressively out of phase except at one wavelength that satisfies the Bragg condition (Othonos et al., 2006):

$$\lambda_B = 2n_{eff}\Lambda \tag{1}$$

where λ_B is the Bragg wavelength, n_{eff} is the effective refractive index of the fibre core at the free space centre wavelength. Λ is the grating period. When the grating period changes (due to strain or temperature), the reflected wavelength changes.

2.1. Coupled mode theory and transfer matrix method

The spectral response of FBGs can be calculated using coupled mode equations and the transfer matrix method. The transfer matrix method is an approximation based method and models the non-uniform grating properties as a piecewise constant function and reduces the calculation of the grating spectral response to a single response matrix (Prabhugoud and Peters, 2004).

FBGs couple light from the core propagating guided mode into the counter propagating guided and cladding modes. This causes loss troughs in the transmission spectrum and peaks in the reflection spectrum (Liau, 2009). Using coupled mode theory, the electric fields of the backward and forward propagating waves can be obtained (Othonos et al., 2006):

$$E_a(x,t) = A(x)exp[i(\omega t - \beta x)] \tag{2}$$

$$E_b(x,t) = B(x)exp[i(\omega t + \beta x)] \tag{3}$$

The complex amplitudes $A(x)$ and $B(x)$ are given by Othonos et al. (2006):

$$\frac{dA(x)}{dx} = i\kappa B(x)exp[-i2(\Delta\beta)x] \tag{4}$$

$$\frac{dB(x)}{dx} = -i\kappa^{*}A(x)exp[i2(\Delta\beta)x] \tag{5}$$

$\Delta\beta = \beta - \beta_0$ is the differential propagation constant. β is the propagation constant given by $\frac{2\pi n_0}{\lambda}$ and $\beta_0 = \pi/\Lambda$. κ is the coupling coefficient and κ^{*} is the complex conjugate. However, for a uniform grating κ is a constant and given by $\kappa = \pi^{*}m^{*}\overline{\delta n_{eff}}/\lambda$ where m is the striate visibility for a single mode FBG. The detuning $\Delta\beta$ which is dependent on z for all gratings is defined as Erdogan (1997):

$$\Delta\beta = \beta - \frac{\pi}{\Lambda} \tag{6}$$

$$\Delta\beta = 2\pi n_0\left(\frac{1}{\lambda} - \frac{1}{\lambda_D}\right) + \frac{2\pi}{\lambda}\overline{\delta n_{eff}} \tag{7}$$

λ_D is the 'design wavelength' for Bragg reflectance by a weak grating where ($\Delta n \rightarrow 0$) and is given by $\lambda_D = 2n_0\Lambda$. $\overline{\delta n_{eff}}$, which is the 'dc' index change spatially averaged over the grating period.

The perturbation of refractive index is given by (Peters et al., 2001):

$$\delta n_{eff}(z) = \overline{\delta n_{eff(z)}}\left\{1 + \nu cos\left[\frac{2\pi}{\Lambda}z + \phi(z)\right]\right\} \tag{8}$$

where $\phi(z)$ is the grating chirp and for a uniform grating $\phi(z) = 0$. In the transfer matrix method the grating is divided into N uniform sections, Δ = L/N, where L is the length of the FBG.

The transfer matrix relationship can be obtained for sections at z and z+Δ. The backward output reflected wave a_z and the forward output transmitted wave $b_{z+\Delta}$ can be expressed using a transfer matrix (Ikhlef et al., 2012):

$$\begin{bmatrix} a_{z+\Delta} \\ b_{z+\Delta} \end{bmatrix} = \begin{bmatrix} cosh(\gamma\Delta) - i\frac{\Delta\beta}{\gamma}sinh(\gamma\Delta) & -\frac{\kappa}{\gamma}sinh(\gamma\Delta) \\ i\frac{\kappa}{\gamma}sinh(\gamma\Delta) & cosh(\gamma\Delta) + i\frac{\Delta\beta}{\gamma}sinh(\gamma\Delta) \end{bmatrix} \cdot \begin{bmatrix} a_z \\ b_z \end{bmatrix} \tag{9}$$

$$\gamma = \sqrt{\kappa^2 - \Delta\beta^2} \tag{10}$$

Connecting all the fields' together:

$$\begin{bmatrix} a_L \\ b_L \end{bmatrix} = T \cdot \begin{bmatrix} a_0 \\ b_0 \end{bmatrix} \tag{11}$$

where $T = T_N{*}T_{N-1}{*}\cdots\cdots{*}T_i{*}\cdots..{*}T_1$T has dimensions 2×2 and can be written as

$$T = \begin{bmatrix} T_{11} & T_{12} \\ T_{21} & T_{22} \end{bmatrix} \tag{12}$$

$$T_i = \begin{bmatrix} cosh(\gamma l_i) - i\frac{\Delta\beta}{\gamma}sinh(\gamma l_i) & -\frac{\kappa}{\gamma}sinh(\gamma l_i) \\ i\frac{\kappa}{\gamma}sinh(\gamma l_i) & cosh(\gamma l_i) + i\frac{\Delta\beta}{\gamma}sinh(\gamma l_i) \end{bmatrix} \tag{13}$$

The reflection coefficient is calculated by:

$$R(\lambda) = \left|\frac{T_{21}(\lambda)}{T_{11}(\lambda)}\right|^2 \tag{14}$$

2.2. Response to a non-uniform strain field

According to Peters *et al.* (Peters et al., 2001) the applied strain induces a change in both grating period and mean refractive index and these two effects can be linearly superimposed at least for a piecewise continuous strain field because it is locally uniform. An effective strain $(1 - p_e)\varepsilon_{zz(z)}$ can be applied to the grating, where $\varepsilon_{zz(z)}$ is the strain

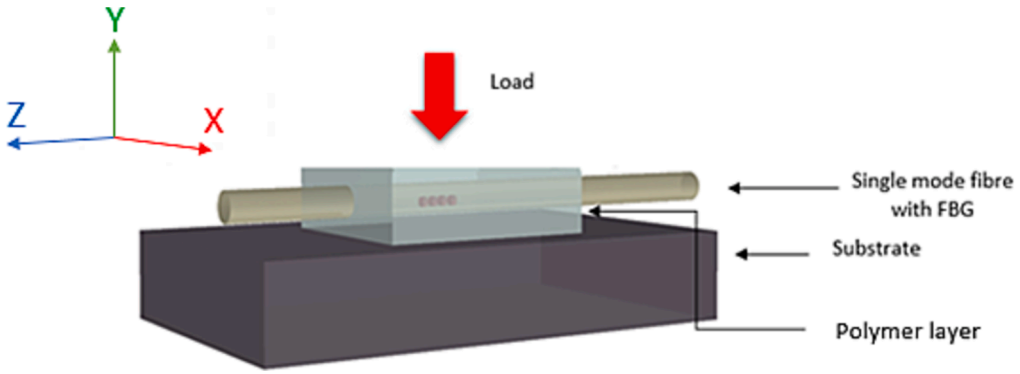

Fig. 1. Schematic illustration of the optical fibre fbg pressure sensor.

variation along the z direction. $p_e = \frac{n_{eff}^2}{2}[p_{12} - \nu(p_{11} + p_{12})]$is the photo elastic coefficient, where, p_{11} and p_{12} are the components of the strain optical fibre sensor and ν is Poisson's ratio of the optical fibre. Thus for a non-uniform grating, the grating period is Peters et al. (2001):

$$\Lambda(z) = \Lambda_0[1 + (1 - p_e)\varepsilon_{zz}(z)] \tag{15}$$

The effective mode index is Peters et al. (2001):

$$\delta n_{eff}(z) = \overline{\delta n_{eff}}\left\{1 + \zeta cos\left[\frac{2\pi}{\Lambda_0[1 + (1 - p_e)\varepsilon_{zz}(z)]}z\right]\right\} \tag{16}$$

where ζ is the fringe visibility. $\zeta \approx 1$ for a conventional single mode fibre (Ling et al., 2007; Chen et al., 2013). The bandwidth of an FBG in a free state is the full width at half maximum (FWHM) bandwidth (Bennion et al., 1996; Pereira et al., 2015):

$$\overline{\lambda_0} \approx \overline{\lambda_{FWHM}} = \lambda_b s[\left(\frac{\delta n_{eff}}{2n_{core}}\right)^2 + (\frac{\Lambda}{L})^2]^{1/2} \tag{17}$$

where $s \approx 1$ for strong gratings with near 100- % reflectivity and $s \approx 0.5$ for weak gratings. n_{core} is the unexposed core refractive index (Bennion et al., 1996). The width variation of the reflected peak resulting from a non-uniform strain effect can be approximated using the maximum ($\varepsilon_{zz}^{max}(z)$) and minimum strain ($\varepsilon_{zz}^{min}(z)$) values along the grating. Thus, the maximum grating period (Λ_{max}) and the minimum grating period (Λ_{min}) can be calculated. The bandwidth of a non-uniform strain is (Pereira et al., 2015):

$$\Delta\lambda_{wv}^{'} = \left[2n_{eff}\Lambda_{max} - 2n_{eff}\Lambda_{min}\right] - \overline{\lambda_{FWHM}} \tag{18}$$

2.3. Birefringence/signal anomalies of FBGs to transverse loading conditions

The refractive index changes caused by applied loads are known as photo-elastic phenomena (Bennion et al., 1996). When an FBG experiences transverse loading it may exhibit birefringence effects causing splitting of the FBG peak signal into two peaks. Birefringence is a condition where two orthogonal components of the optical fibre cross section have different refractive indices (Pereira et al., 2015). When an FBG is under transverse loading in the compressed side (slow axis) the refractive index will increase and in the orthogonal direction (fast axis) it will decrease. In any unloaded FBG the refractive index is assumed uniform across the core cross section at any location in the fibre axis. When a transverse load is applied to the FBG, the core cross section of the FBG will deform into an elliptical shape with a compressive force acting along the y-axis, Fig. 1. Photo elastic induced refractive index changes in the x and y polarisation axes are Mastero (2005):

$$(\Delta n_{eff})_x = -\frac{(n_{eff})^3}{2E} \times \{(p_{11} - 2\nu p_{12})\sigma_x + [(1 - \nu)p_{12} - \nu p_{11}] \times [\sigma_y + \sigma_z]\} \tag{19}$$

$$(\Delta n_{eff})_y = -\frac{(n_{eff})^3}{2E} \times \{(p_{11} - 2\nu p_{12})\sigma_y + [(1 - \nu)p_{12} - \nu p_{11}] \times [\sigma_x + \sigma_z]\} \tag{20}$$

where σ_x, σ_y and σ_z are the stress components along x, y and z direction

The corresponding Bragg wavelength changes are given by Mastero (2005):

$$(\Delta\lambda_B)_x = -\frac{(n_{eff})^3\Lambda_{B,0}}{E} \times \{(p_{11} - 2\nu p_{12})\sigma_x + [(1 - \nu)p_{12} - \nu p_{11}] \times [\sigma_y + \sigma_z]\} + 2\frac{n_{eff}\Lambda_{B,0}}{E} \times \{\sigma_z - \nu[\sigma_x + \sigma_y]\} \tag{21}$$

Table 1
Modelling parameters.

Parameter	Value
FBG length	3 mm
Design wavelength / Un-deformed wavelength	1549.1 nm
Initial effective refractive index	1.4465
Bandwidth limits	1539.1—1559.1 nm
Resolution	1500 points
Strain optic tensor coefficients	$P_{11} = 0.121$ $P_{12} = 0.27$
Poisson's ratio of the fibre	0.17
Young's Modulus of fibre	71.7e9 Pa
Young's Modulus of polymer layer	143 MPa
Poisson's ratio of polymer layer	0.4
Young's Modulus of the base	210 GPa
Poisson's ratio of the base	0.3
Peak value of the dc effective index of refraction	5e-5
Number of sections for T-matrix calculations	300
Power coupling coefficients	Px = 0.85 Py = 0.15

$$(\Delta\lambda_B)_y = -\frac{(n_{eff})^3\Lambda_{B,0}}{E} \times \{(p_{11} - 2\nu p_{12})\sigma_y + [(1 - \nu)p_{12} - \nu p_{11}] \times [\sigma_x + \sigma_z]\} + 2\frac{n_{eff}\Lambda_{B,0}}{E} \times \{\sigma_z - \nu[\sigma_x + \sigma_y]\} \tag{22}$$

The bandwidth variation of the reflected peak due to the transverse deformation is obtained by observing from equation 23 and 24 that the first terms of the equations are different and correspond to the effect of transverse applied loads and the second terms of these equations are identical and correspond to the Bragg reflection wavelength changes of the FBG induced by longitudinal strain. Therefore the Bragg wavelength width variation of the reflected peak due to transverse loading is Mastero (2005):

$$\Delta\lambda_{WV} = \Delta\lambda_{wv}^{'} + \Delta\lambda_{wv}^{''} \tag{23}$$

Where, $\Delta\lambda_{wv}^{'} = 2\Lambda\left|\Delta n_{effx} - \Delta n_{effy}\right|$ and $\Delta\lambda_{wv}^{''} = \frac{\Lambda n_0^3}{E_f}\left[(1 + v_f)(p_{12} - p_{11})\right]\left|\sigma_x - \sigma_y\right|$

The wavelength shift is:

$$\Delta\lambda_b = \lambda_b * (1 - p_e) * (average\,(\varepsilon_{zz}(z)) \tag{24}$$

where λ_b is the design wavelength of the FBG or the Bragg wavelength in un-deformed conditions.

Since the gratings seen by the orthogonal polarisation states are independent, the total reflectivity can be deduced by adding the weighted reflectivity along each polarisation state. The reflectivity weights of the two different polarisation states are defined by the intensity fractions present in each direction. Therefore total reflectivity is Michaille et al. (2003):

$$R = p_x^2 R_x + p_y^2 R_y \tag{25}$$

p_x and p_y are the amplitude components along x and y axes where $p_x^2 + p_y^2 = 1$.

3. Method

3.1. Model construction

The FBG simulation structure can be divided into two steps. Finite element analysis for the stress and strain modelling across the FBG due to the pressure loading and transfer matrix formulism for the modelling of the FBG reflectivity spectrum due to the stress and strain experienced by the FBG. FEA analysis is performed using ABAQUS FEA, Dassault

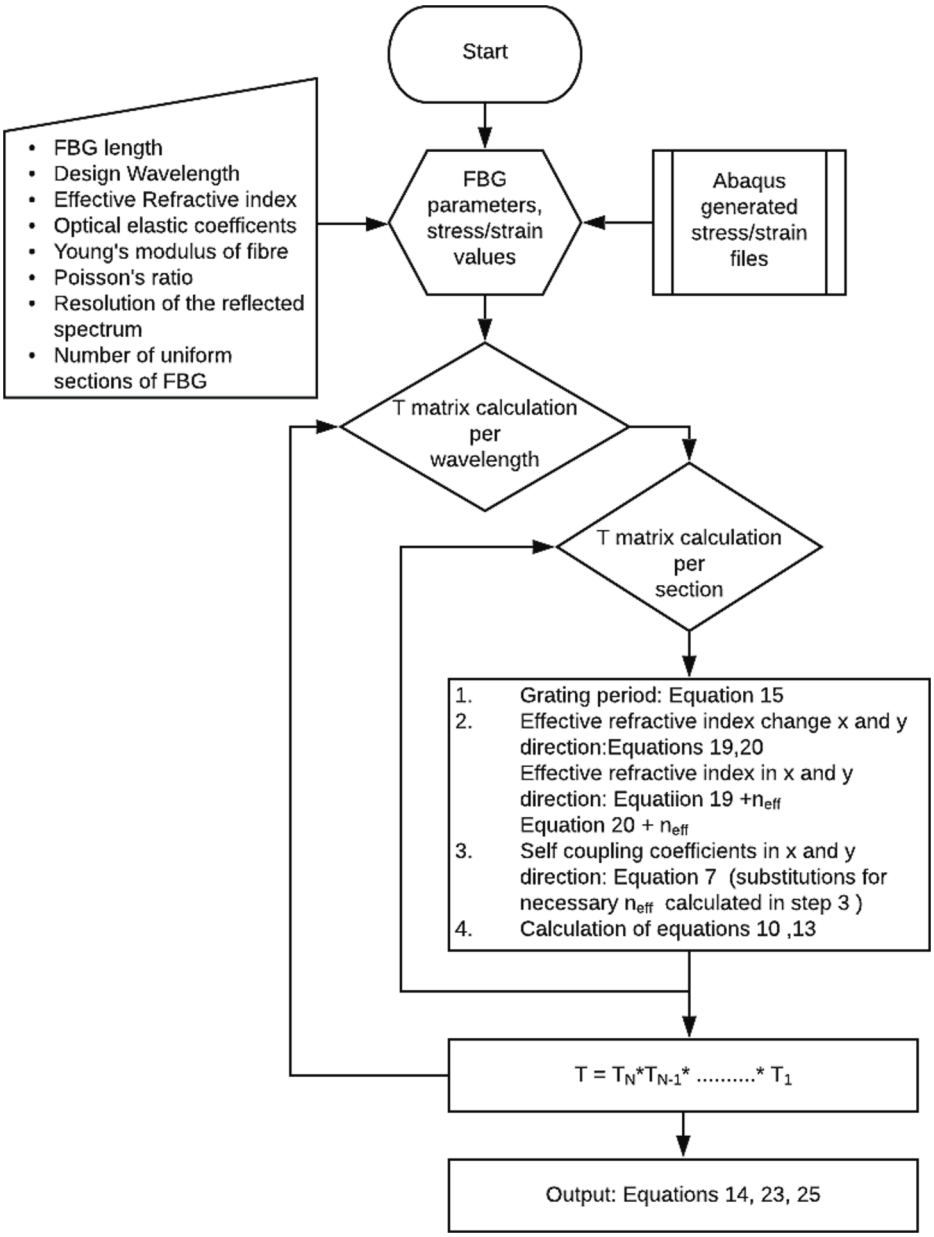

Fig. 2. FBG simulation flow chart.

Systèmes Simulia Corp., USA and the transfer matrix formulism using MATLAB, MathWorks, USA.

3.1.1. FEA modelling and data extraction

The FEA modelling consists of:

1) *Creation of parts and assigning each part material properties*: The model consists of an optical fibre, polymer layer and a base (Fig. 1). Each of the parts was assumed to be deformable and is assigned with their Young's modulus and Poisson's ratio as shown in Table 1.
2) *Optimisation of mesh parameters*: Mesh density is an important parameter used to achieve accuracy. A high density mesh will usually produce more accurate results, however, if a mesh is too dense it will require long run times, especially in nonlinear analyses. In this work, the optimum mesh size of 0.01 mm was selected.
3) *Creation of assembly and selection of contact algorithm and boundary conditions, selection of geometric non-linearity*: ABAQUS provides two different contact algorithms - general contact and contact pairs, which share many underlying algorithms. Nevertheless, the contact interaction domain, contact properties and surface attributes are specified independently for general contact, offering a more flexible way to add detail incrementally to a model. In this work, the general contact algorithm was utilised for its convenience and accuracy. An adhesive type bonding is used between the optical fibre and the polymer layer, therefore, a tie constrain was introduced between the outer surface of the fibre and the inner surface of the polymer layer so that there is no relative motion.
4) Stress and strain profiles of the fibre are written to text files for each FEM simulation. These files are later exported to MATLAB for the transfer matrix formulism.

3.1.2. FBG simulation algorithm structure

Fig. 2 illustrates a flow chart of the algorithm structure used to simulate the FBG response. For each wavelength determined by the bandwidth and the resolution inputs, reflectivity is calculated. The number of sections used for the transfer matrix is determined by the

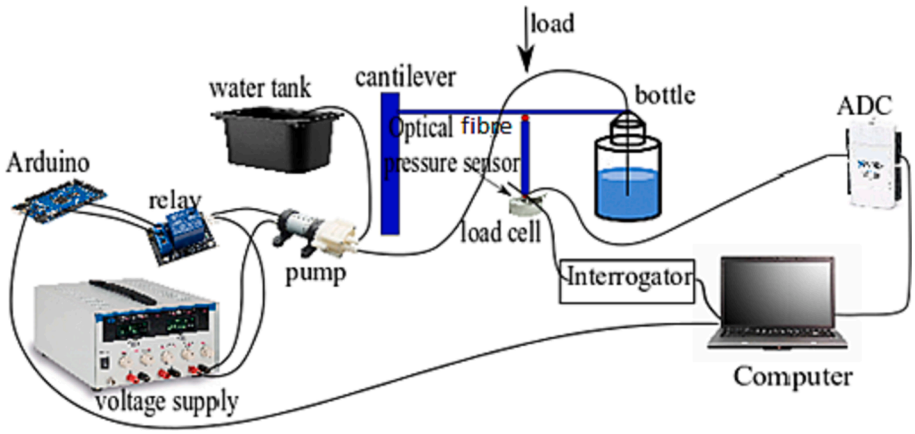

Fig. 3. Experimental validation setup (ADC – analogue to digital converter).

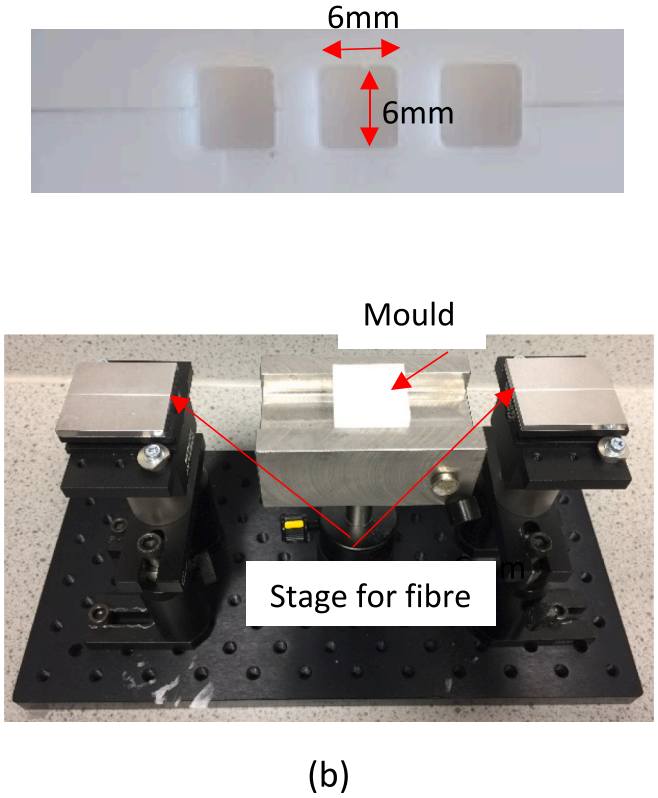

Fig. 4. (a) Picture of the 3D printed mould used to fabricate the sensor (b) the curing setup.

mesh resolution of the FEA model. For example, if the FBG is 3 mm long and the fibre is meshed with 0.01 mm resolution, there are 300 mesh elements in the FBG. Transfer matrix calculations are performed for each wavelength section for the 300 sections.

3.2. Experimental validation setup

The experimental validation setup (Fig. 3, figure S1) consists of a customized cantilever that applies a known load to the FBG pressure sensor using a vertical rod connected to it. The optical fibre pressure sensor is connected to an interrogator (SmartScan, Smart Fibres Ltd., UK). A load cell (FC23 Compression Load Cell, TE Ltd., USA) was placed on a stage beneath the optical fibre sensor to monitor the pressure applied. The signal of the load cell converted to a digital signal using an

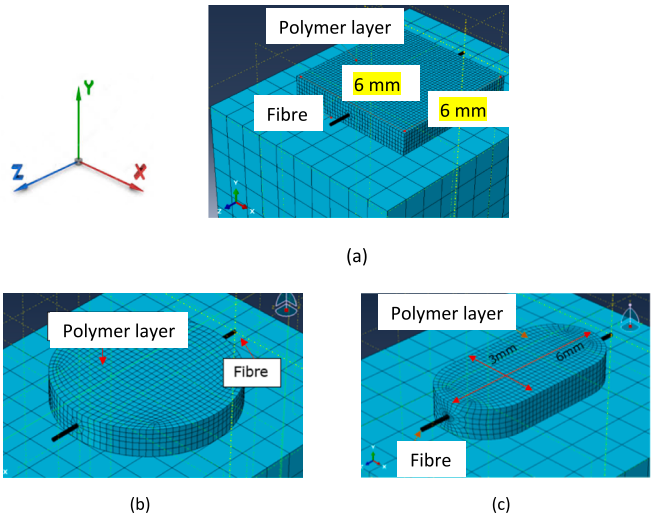

Fig. 5. FEA mesh model of the FBG (3 mm) embedded in (a) 6 mm × 6 mm × 1 mm cuboid shape (b) 6 mm diameter, 1 mm thickness polymer disc (c) a quasi-rectangular shape (6 mm × 3 mm × 1 mm).

analogue to digital converter (National Instruments, USA).

A bottle connected to a water pump is hung at the distal end of the cantilever. The pump flow rate is controlled by an Arduino development board (Arduino UNO, Italy) which controls the load applied. The water pump is kept on for 5 s during filling with a delay of 180 s to stabilise the signal. The whole measurement procedure was repeated three times.

3.2.1. Embedment of the FBG in polymer layer

Fig. 4 (a) shows a picture of the 3D printed mould (6 mm × 6 mm × 1 mm) used to fabricate the sensor. This mould is made from PTFE (Polytetrafluoroethylene) resin. The unstripped region of the optical fibre sits in the mould groove while the stripped region, where the FBG is located, is centered around the square well. The fibre is secured at both ends using magnets to maintain some axial strain in the fibre avoiding bending (Fig. 4 (b)). The polymer based adhesive is then poured into the mould. The polymer layer (acrylic adhesive, Loctite AA 3926, Henkel, Germany) is cured for 5 min with a 5 W UV lamp (wavelength range 365 – 370 nm).

3.3. Investigation of the pressure sensor response

Initially, experimental validation was performed for the simulation results produced for a polymer layer of cuboid shape with dimensions of

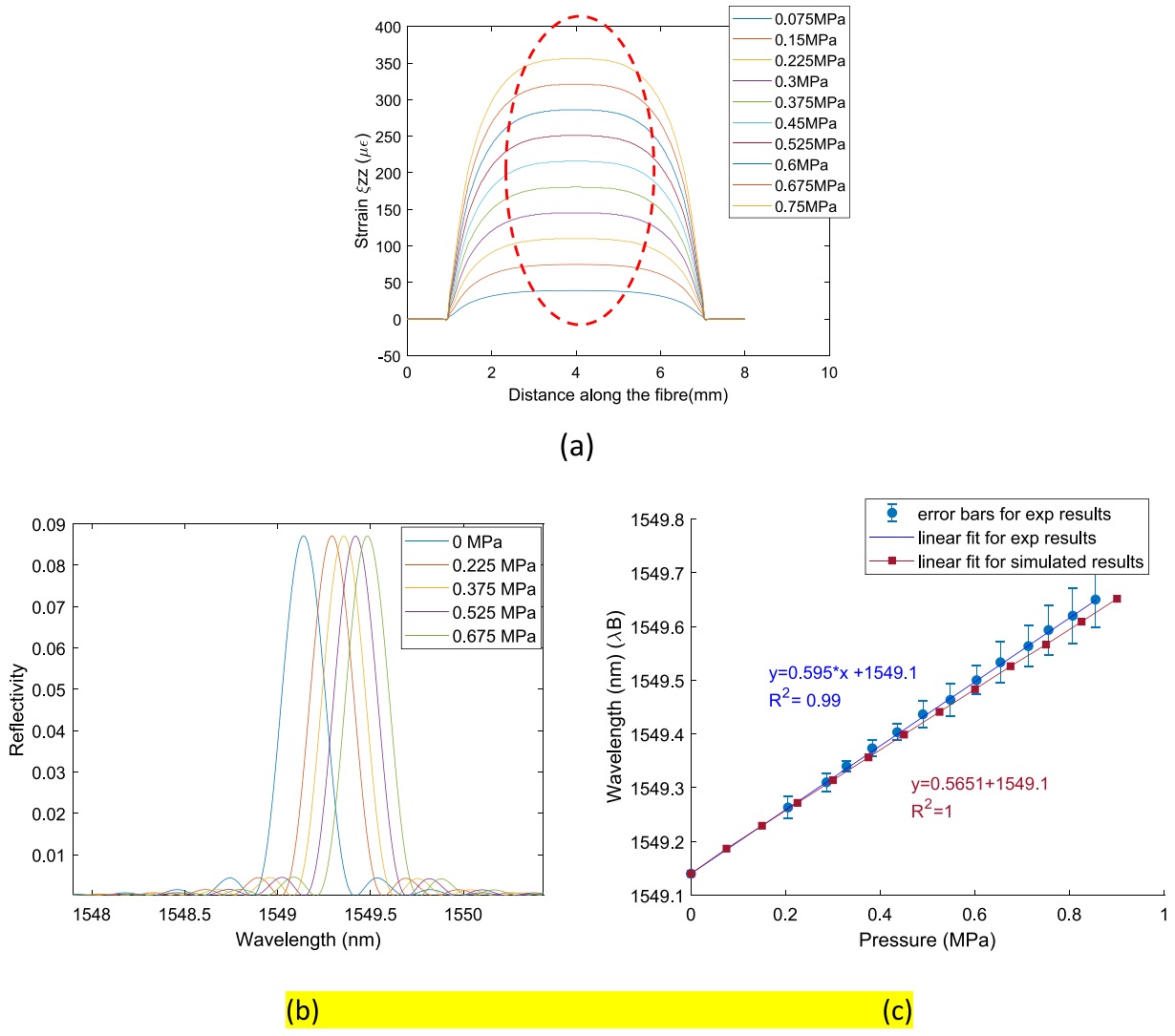

Fig. 6. (a) The strain transferred to the axis of the fibre from the uniform transverse loading plotted over the distance along the fibre. The FBG is located between 2.5 mm and 5.5 mm which lie inside the dashed red ellipse (b) Reflection spectra of the FBG (3 mm) embedded in a cuboid shaped polymer layer (6 mm × 6 mm × 1 mm) at the centre of the layer. Young's modulus of the layer is 143 MPa (c) Bragg wavelength sensitivity to the applied transverse pressure load for experimental and simulated results. (For interpretation of the references to colour in this figure legend, the reader is referred to the web version of this article.)

6 mm × 6 mm × 1 mm. The FBG is 3 mm long and situated at the centre of the polymer layer. The parameters used for the FEA modelling and FBG modelling are listed in Table 1.

The experimental validation is followed by optimisation of the shape. Three different shapes including a cuboid (6 mm × 6 mm × 1 mm), quasi rectangle (6 mm × 3 mm × 1 mm) and circular disc (diameter 6 mm) have been compared. The FEA meshed models used for the simulations are illustrated in Fig. 5. The Young's modulus, thickness, strain optic coefficients and fibre parameters are constant throughout all the simulations.

Once the optimised shape is recognised as the disc (section 4.2), the next set of simulations were performed to optimise the dimensions. Three different disc diameters (6 mm, 5.5 mm and 7 mm) are compared.

Subsequently, by optimising the shape and dimensions (disc shape with 5.5 mm diameter and thickness 1 mm), the next step is to identify the optimum material properties. Three different Young's moduli which are commercially available were simulated in order to identify the optimum material. The used materials are Loctite AA 3926 (Henkel, Germany) with Young's modulus of 143 MPa, Panacol Vitralit 1655 (Panacol Adhesives, Frankfurt, Germany) adhesive with a Young's modulus of 44 MPa and Loctite AA3921 (Henkel, Germany) with a Young's modulus of 20 MPa.

4. Results

4.1. Experimental validation

Fig. 6 (a) depicts the simulated results for axial strain distibution experienced by the axis of the fibre. The polymer layer lies in between 1 mm and 7 mm range along the x axis of the graph and the FBG between 2.5 mm and 5.5 mm. The maximum strain is observed in this region. Fig. 6(b) shows the evolution of the simulated reflection spectra to the uniform transverse pressure load. The Bragg peak shifts to the red end of the wavelength spectrum with increasing transverse pressure loading. The results obtained from the experimental validation have been plotted with the simulated result obtained on the same graph shown in Fig. 6 (c), figure S2. The experimentally obtained Bragg wavelength sensitivity is 0.595 nm/MPa, and the simulated results agree well (R^2 = 0.99). Moreover, the simulated results always lie within the error limits of the experimentally obtained results.

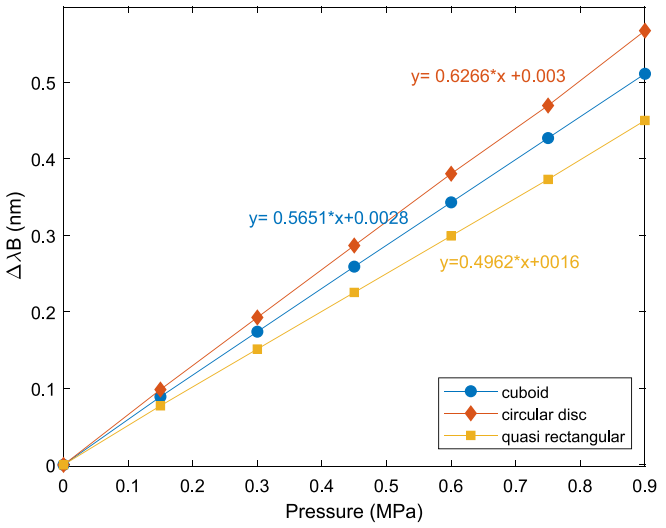

Fig. 7. Simulated results of pressure sensitivity of Bragg peak to different transverse loading for 3 different shapes, cuboid (6 mm × 6 mm × 1 mm), disc (6 mm diameter, 1 mm thick), quasi rectangle (6 mm × 3 mm × 1 mm).

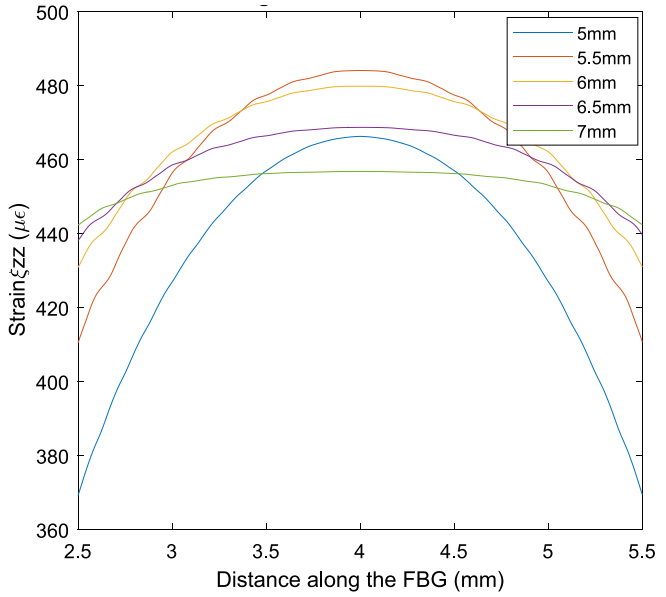

Fig. 8. Simulated results of longitudinal strain along the FBG for different diameter layers for 0.9 MPa transverse loading.

4.2. Pressure sensitivity for different shapes

The simulated wavelength sensitivity of the Bragg peak, plotted for the three different shapes are illustrated in Fig. 7. The highest sensitivity was observed for the circular disc with 6 mm diameter.

4.3. Pressure sensitivity for different diameters of the circular shaped polymer layer

Since the highest sensitivity for the simulated results is obtained for the disc, the optimum diameter for the disc layer was investigated. Fig. 8 illustrates the axial strain along the FBG for circular layers with diameter range of 5–7 mm, for a pressure of 0.9 MPa.

According to Fig. 8, it is clear that the maximum strain transfer and hence, the maximum sensitivity, occurs at a diameter of 5.5 mm.

The Bragg wavelength sensitivity to transverse loading is plotted for diameters 5.5 mm, 6 mm and 7 mm (Fig. 9). The highest sensitivity is achieved for a diameter of 5.5 mm although there is a very small difference for each case.

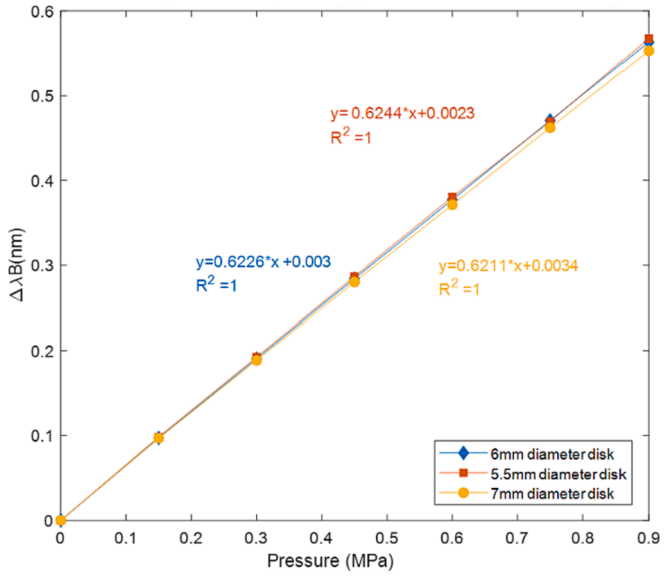

Fig. 9. Simulated results of pressure sensitivity of Bragg peak to different transverse loading for 3 different diameters (6 mm, 5.5 mm and 7 mm).

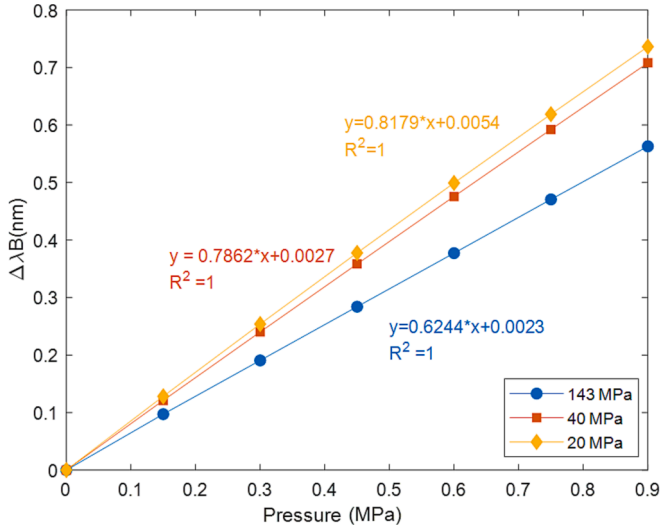

Fig. 10. Simulated results of pressure sensitivity of Bragg peak to different transverse loading for 5.5 mm diameter disc with 1 mm thickness for three different Young's moduli (143 MPa, 40 MPa, 20 MPa).

4.4. Pressure sensitivity with Young's modulus

Since the highest sensitivity was achieved for the 5.5 mm diameter disc with 1 mm thickness, this shape has been used for the simulations for three different Young's moduli (143 MPa, 40 MPa and 20 MPa).

Fig. 10 compares the wavelength sensitivity of the Bragg peak for the 5.5 mm diameter, 1 mm thick polymer layer for the three different Young's moduli. The highest observed sensitivity is 0.8179 nm/MPa for the 20 MPa Young's modulus and this is 1.04 times the sensitivity of the 44 MPa Young's modulus layer and 1.31 times the sensitivity of the 143 MPa Young's modulus layer.

5. Discussion

When an FBG is embedded in a polymer layer, the axial strain profile experienced by the FBG is heavily dependent on the strain transfer efficiency of the layer to the FBG (Zhou et al., 2010; Pak, 1992; Sun et al., 2007, 2016). This depends on many polymer layer parameters such as thickness, bonding length, material properties and shape. However, the maximum strain transfer is achieved when the FBG is positioned at the centre of the xz plane of the polymer layer as the axial strain is maximum at this position.

The highest sensitivity is observed for the disc shape among the three shapes. As the cross sectional area increases the transverse force acting on the patch also increases for a particular uniform pressure load. Therefore the cuboid shape and the disc shape have higher pressure sensitivities than the quasi rectangular shape. However, the disc has higher sensitivity than the cuboid which may be due to the radial symmetry of the disc as the radial stresses contribute towards the axial strain experienced by the FBG.

Fig. 8 shows the axial strain along the FBG for circular layers with different diameters for a pressure of 0.9 MPa. The maximum strain experienced at the centre of the FBG clearly depends on the disc diameter with a maximum transfer observed for the 5.5 mm diameter disc. The deformation of the polymer layer due to the transverse load produces reaction forces on the fibre and hence produces longitudinal stresses. This reaction forces increase with the increase of the diameter of the polymer layer as the bonded length increases. When the diameter is less than 5.5 mm the reaction forces are dominant when compared to the increase in area of the layer, and hence the net longitudinal stress increases. Above the optimum diameter (5.5 mm) the area increase due to the increase of diameter is dominant when compared to the reaction forces and hence the stresses and net longitudinal strain start to reduce.

As the Young's modulus of the material decreases the polymer layer becomes more deformable and hence the reaction forces applied on the fibre increases. As a result of the longitudinal strain increases, the Bragg wavelength shift is greater for the same pressure load, when compared to higher Young's modulus (less deformable) materials. Therefore, the wavelength sensitivity to transverse load increases.

The reflection spectra of all the simulated FBGs embedded in different polymer layers showed no birefringence due to the applied transverse loading within the observed pressure range (<1 MPa). Simulations (see supporting data, Figures S3-S7) demonstrate that this typically can be observed at ~ 3 Mpa. The application of the pressure sensor is within this pressure range and the effects out of this range are less important and out of the scope of this study. This is due to transverse stresses being negligible compared to the longitudinal strain within the considered pressure range. Therefore, the refractive index is uniform about the axis of the fibre and hence the reflected peak does not separate along the x and y axes.

6. Conclusions

A mathematical model for a highly sensitive optical fibre Bragg grating pressure sensor embedded in a polymer layer for contact pressure measurement in health care applications has been demonstrated. The mathematical model was validated experimentally for a 3 mm long FBG embedded in a 6 mm × 6 mm × 1 mm polymer cuboid layer with a Young's modulus of 143 MPa.

Three different shapes including cuboid, quasi rectangular and circular disc have been simulated to obtain the optimum shape and size for the sensor. According to the simulation results, a disc of diameter 5.5 mm shows the highest sensitivity. The effect of the Young's modulus on the sensitivity of the FBG was also investigated with the highest sensitivity observed for a 5.5 mm disc with 1 mm thickness and a Young's modulus of 20 MPa.

The change in polymer layer design, increased the sensitivity 1.5 times over the original design and by ~ 270 times of a bare FBG.

CRediT authorship contribution statement

C.L. Abeywardena: Data curation, Formal analysis, Funding acquisition, Writing – original draft. **Q. Zhang:** Data curation, Formal analysis, Methodology. **S. Korposh:** Conceptualization, Funding acquisition, Methodology, Writing – review & editing. **S.P. Morgan:** Conceptualization, Funding acquisition, Methodology, Writing – review & editing. **S. Bull:** Conceptualization, Funding acquisition, Methodology, Writing – review & editing. **R. Correia:** Conceptualization, Funding acquisition, Supervision, Writing – review & editing.

Declaration of competing interest

The authors declare that they have no known competing financial interests or personal relationships that could have appeared to influence the work reported in this paper.

Data availability

Data will be made available on request.

Acknowledgements

The authors acknowledge support from the EPSRC Medical Devices and Vulnerable Skin Network (EP/N02723X/1).

Appendix A. Supplementary data

Supplementary data to this article can be found online at https://doi.org/10.1016/j.rio.2024.100604.

References

Barbenel, J.C., Sockalingham, S., 1990. Device for measuring soft tissue interface pressures. J. Biomed. Eng. 12 (6), 519–522.
Bennion, I., Williams, J.A.R., Zhang, L., Sugden, K., Doran, N.J., 1996. UV-written in-fibre Bragg gratings. Opt. Quant. Electron. 28 (2), 93–135.
Bhattacharya, S., Mishra, R., 2015. Pressure ulcers: Current understanding and newer modalities of treatment. Indian J. Plastic Surg. 48 (1), 4–16. Medknow Publications.
Buis, A.W.P., Convery, P., 1997. Calibration problems encountered while monitoring stump/socket interface pressures with force sensing resistors: Techniques adopted to minimise inaccuracies. Prosthet. Orthot. Int. 21 (3), 179–182.
Chen, L., et al., 2020. Ultrahigh-sensitivity label-free optical fiber biosensor based on a tapered singlemode- no core-singlemode coupler for Staphylococcus aureus detection. Sens. Actuators B 320, 128283.
Chen, Y., Li, J., Yang, Y., Chen, M., Li, J., Luo, H., 2013. Numerical modeling and design of mid-infrared FBG with high reflectivity. Optik (stuttg) 124 (16), 2565–2568.
"Compression in venous leg ulcers a WUWHS consensus document - Wounds International." [Online]. Available: https://www.woundsinternational.com/resources/details/compression-venous-leg-ulcers-wuwhs-consensus-document. [Accessed: 21-Jan-2020].
Correia, R., et al., 2016. Highly sensitive contact pressure measurements using FBG patch in endotracheal tube cuff. Sixth Eur. Work. Opt. Fibre Sensors 9916, 99161F.
Correia, R., et al., 2021. Intra-tracheal multiplexed sensing of contact pressure and perfusion. Biomed. Opt. Express 13, 48–64.
Correia, R., Chehura, E., James, S.W., Tatam, R.P., 2006. Locally pressed fibre Bragg grating pressure sensor. In: Optics InfoBase Conference Papers, p. TuE32.
Correia, R., Chehura, E., James, S.W., Tatam, R.P., 2007. A pressure sensor based upon the transverse loading of a sub-section of an optical fibre Bragg grating. Meas. Sci. Technol. 18 (10), 3103–3110.
Correia, R., Chehura, E., Li, J., James, S.W., Tatam, R.P., 2010. Enhanced sensitivity fibre Bragg grating (FBG) load sensor. Meas. Sci. Technol. 21.
Correia, R., James, S., Lee, S.-W., Morgan, S.P., Korposh, S., 2018. Biomedical application of optical fibre sensors. J. Opt. 20 (7), 073003.
Culshaw, B., 2006. The optical fibre Sagnac interferometer: an overview of its principles and applications. Meas. Sci. Technol. 17, R1.
Dealey, C., Posnett, J., Walker, A., 2012. The cost of pressure ulcers in the United Kingdom. J. Wound Care 21 (6), 261–266.
Erdogan, T., 1997. Fiber grating spectra. J. Light. Technol. 15 (8), 1277–1294.
"European Wound Management Association (EWMA). Understanding compression therapy. Position Document.," 2003. [Online]. Available: https://ewma.org/fileadmin/user_upload/EWMA.org/Position_documents_2002-2008/Compression.pdf. [Accessed: 21-Jan-2020].
Ferguson-Pell, M., Hagisawa, S., Bain, D., 2000. Evaluation of a sensor for low interface pressure applications. Med. Eng. Phys. 22 (9), 657–663.

Gafsi, R., El-Sherif, M.A., 2000. Analysis of Induced-Birefringence Effects on Fiber Bragg Gratings. Opt. Fiber Technol. 6 (3), 299–323.
Guest, J.F., Fuller, G.W., Vowden, P., 2018. Venous leg ulcer management in clinical practice in the UK: costs and outcomes. Int. Wound J. 15 (1), 29–37.
Hassoon, O., Tarfoui, M., a El Malk, 2015. Numerical simulation of fiber bragg grating spectrum for mode-I delamination detection. Int. J. Mech. Aerospace, Ind. Mechatronics Eng. 9 (1), 144–149.
Hernandez, F.U., et al., 2017. Optical fibre sensing during critical care. vol. 10340. In: International Conference on Biophotonics V, p. 1034012.
Hu, H., Li, S., Wang, J., Wang, Y., Zu, L., 2016. FBG-based real-time evaluation of transverse cracking in cross-ply laminates. Compos. Struct. 138, 151–160.
Ikhlef, A., Hedara, R., Chikh-bled, M., 2012. Uniform Fiber Bragg Grating modeling and simulation used matrix transfer method. Int. J. Comput. Sci. Issues 9 (1), 368–374.
Jonsson, A., Lindén, M., Lindgren, M., Malmqvist, L.Å., Bäcklund, Y., 2005. Evaluation of antidecubitus mattresses. Med. Biol. Eng. Compu. 43 (5), 541–547.
Liau, J.-J., et al., 2009. A new look at numerical analysis of uniform fiber bragg gratings using coupled mode theory. Prog. Electromagn. Res. 93, 385–401.
Ling, H.Y., Lau, K.T., Jin, W., Chan, K.C., 2007. Characterization of dynamic strain measurement using reflection spectrum from a fiber Bragg grating. Opt. Commun. 270 (1), 25–30.
Magalhaes, M.G., et al., 2007. Risk factors for pressure ulcers in hospitalized elderly without significant cognitive impairment. Wounds 19 (1), 20–24.
Margolis, D.J., Bilker, W., Santanna, J., Baumgarten, M., 2002. Venous leg ulcer: Incidence and prevalence in the elderly. J. Am. Acad. Dermatol. 46 (3), 381–386.
Mastero, S., 2005. Optomechanical behavior of embedded fiber Bragg grating strain sensors. Drexel University. PhD Thesis.
Michaille, L., McCall, M.W., Lai, Y.C., Williams, J.A.R., 2003. Analysis of single and multiple, non-permanent, tunable, birefringent spectral holes in a fibre-Bragg grating stop-band produced via uniaxial pressure. Opt. Commun. 222 (1–6), 1–8.
Moo, E.K., Abu Osman, N.A., Pingguan-Murphy, B., Wan Abas, W.A.B., Spence, W.D., Solomonidis, S.E., 2009. Interface pressure profile analysis for patellar tendon-bearing socket and hydrostatic socket. Acta Bioeng. Biomech. 11 (4), 37–43.
Morgan, S.P., et al., 2019. Optical fiber sensors for monitoring in critical care. In: In 2019 41st Annual International Conference of the IEEE Engineering in Medicine and Biology Society (EMBC), pp. 1139–1143.
Othonos, A., Kalli, K., Pureur, D., Mugnier, A., 2006. Fibre Bragg gratings. Springer Ser. Opt. Sci. 123, 189–269.
Pak, Y.E., 1992. Longitudinal shear transfer in fiber optic sensors. Smart Mater. Struct. 1 (1), 57–62.
Partsch, H., et al., 2006. Measurement of lower leg compression in vivo: Recommendations for the performance of measurements of interface pressure and stiffness. Dermatologic Surg. 32 (2), 224–233.
Pereira, G., McGugan, M., Mikkelsen, L.P., 2016. FBG_SiMul V1.0: Fibre Bragg grating signal simulation tool for finite element method models. SoftwareX 5, 163–170.
Pereira, G.F., Mikkelsen, L.P., McGugan, M., 2015. Crack detection in fibre reinforced plastic structures using embedded fibre bragg grating sensors: Theory, model development and experimental validation. PLoS One 10 (10), 1–36.
Peters, K., Studer, M., Botsis, J., Iocco, A., Limberger, H., Salathé, R., 2001. Embeded optical fiber bragg grating sensor in a nonuniform strain field: Measurements and simulations. Exp. Mech. 41 (1), 19–28.
Pfisterer, L., König, G., Hecker, M., Korf, T., 2014. Pathogenese der varizenbildung - Lehren aus der biomechanik. Vasa – J. Vasc. Dis. 43 (2), 88–99. Verlag Hans Huber AG.
Pirouzi, G., Abu Osman, N.A., Eshraghi, A., Ali, S., Gholizadeh, H., Wan Abas, W.A.B., 2014. Review of the socket design and interface pressure measurement for transtibial prosthesis. Scientific World J. 2014. Hindawi Publishing Corporation.
Prabhugoud, M., Peters, K., 2004. Modified Transfer Matrix Formulation for Bragg Grating Strain Sensors. J. Light. Technol. 22 (10), 2302–2309.
Quesada, P., Skinner, H.B., 1991. Department of Veterans Affairs Analysis of a below-knee patellar tendon-bearing prosthesis: A finite element study. J. Rehabil. Res. Dev. 28 (3), 1–12.
Rana, S., Kandadai, N., Subbaraman, H., 2022. Experimental validation of a reflective long period grating design methodology. Results in Optics 7, 100224.
Shao, L., et al., 2019. High-sensitivity temperature sensor based on polarization maintaining fiber Sagnac loop. Photonic Sens 9, 25–32.
Steinberg, M.D., Cooke, E.D., 1993. Design and evaluation of a device for measurement of interface pressure. J. Biomed. Eng. 15 (6), 464–468.
Sun, L., Liang, D., Zhang, H., Li, H., Wang, X., 2007. Comparison of several strain transfer theory calculation methods of the embedded FBG strain sensors. vol. 6423. In: International Conference on Smart Materials and Nanotechnology in Engineering, p. 64233Z.
Sun, L., Hao, H., Zhang, B., Ren, X., Li, J., 2016. Strain Transfer Analysis of Embedded Fiber Bragg Grating Strain Sensor. J. Test. Eval. 44 (6), 20140388.
Touman, A.A., Stratakos, G.K., 2018. Long-term complications of tracheal intubation. Tracheal Intubation. INTECH.
Wang, D.-H.-C., Blenman, N., Maunder, S., Patton, V., Arkwright, J., 2013. An optical fiber Bragg grating force sensor for monitoring sub-bandage pressure during compression therapy. Opt. Express 21 (17), 19799.
Wong, R.Y.-N., Juan, D.H.J., Ibsen, M., Shum, P.P., 2019. Optical fibre long-period grating sensors operating at and around the phase matching turning point. In: Christian Cuadrado-Laborde (Ed.), Applications of Optical Fibers for Sensing.
Wu, Q., et al., 2021. Singlemode-multimode-singlemode fiber structures for sensing applications—A Review. IEEE Sens. J. 21 (11), 12734–12751.
Xu, M.G., Reekie, L., Chow, Y.T., Dakin, J.P., 1993. Optical in-fibre grating high pressure sensor. Electron. Lett 29 (4), 398–399.
Zhou, J., Zhou, Z., Zhang, D., 2010. Study on strain transfer characteristics of fiber Bragg grating sensors. J. Intell. Mater. Syst. Struct. 21 (11), 1117–1122.